Controllable Defect Redistribution of ZnO Nanopyramids with Exposed {10$\bar{1}$1} Facets for Enhanced Gas Sensing Performance

Zhihua Wang, Jie Xue, Dongmei Han, and Fubo Gu*

State Key Laboratory of Chemical Resource Engineering, Beijing University of Chemical Technology, Beisanhuandonglu 15hao, Beijing 100029, China

S *Supporting Information*

ABSTRACT: ZnO nanopyramids (NPys) with exposed crystal facets of {10$\bar{1}$1} were synthesized via a one-step solvothermal method, having a uniform size with a hexagonal edge length of ∼100 nm and a height of ∼200 nm. Technologies of XRD, TEM, HRTEM, Raman, PL, and XPS were used to characterize the morphological and structural properties of the products, while the corresponding gas sensing properties were determined by using ethanol as the target gas. For the overall goal of defect engineering, the effect of aging temperature on the gas sensing performance of the ZnO NPys was studied. The test results showed that, at the aging temperature of 300 °C, the gas sensing property has been improved to the best, with the fast response-recovery time and the excellent selectivity, because the ZnO_{300} has the most electron donors for absorbing the largest content of O^{2-}. Model of defect redistribution was used to explicate the changing of the surface defects at different aging temperatures. The findings showed that, in addition to V_O, Zn_i was the dominant defect of the {10$\bar{1}$1} crystal facet. The gas sensing performance of the ZnO NPys was determined by the contents of V_O and Zn_i, with all of the defects redistributed on the surface. All of the results will be noticeable for the improvement of the sensing performance of materials with special crystal facet exposing.

KEYWORDS: *ZnO, nanopyramid, crystal facet, surface defect, gas sensing*
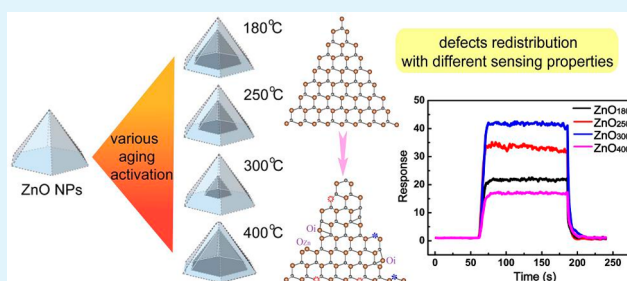
1. INTRODUCTION

ZnO nanomaterials, with a high band gap of 3.37 eV and a large exciton binding energy of 60 meV, were used widely in solar cells, UV lasing devices, photocatalysts, gas sensors, wherein crystal facet exposing and defect distributions play important roles in their performances.[1−4] Among them, gas sensors have become more and more important for detecting VOCs for environmental and security purposes.[3,5] Many efforts have been made to improve the gas sensitivity and selectivity of ZnO sensors by optimizing their morphologies and crystal structures, such as nanofibers,[3] nanorods,[2,5] and nanoflakes.[6] As ZnO nanopyramids (NPys) were a material with particular crystal facets exposing of the {10$\bar{1}$1} facet, they should be a promising candidate for gas sensing. However, because the {10$\bar{1}$1} facet has a high surface energy and a fast growth rate, it is difficult to synthesize the materials with this facet exposing, and there are severely few applications of these materials as gas sensors.[7] Hence, nonaqueous synthesis has become a hot point, as it is capable of preparing nanocrystals with small sizes and particular crystal facets exposing.[8,9] Also, compared with the aqueous methods, this approach is more convenient and less time-consuming. Thus, it has been widely used to control nanostructures with special morphologies for several years.[10−12] In this study, ZnO NPys were synthesized via a nonaqueous method, using oleylamine as a surfactant. The products would be of a narrow size distribution, with the

particular crystal facets of the {10$\bar{1}$1}. Furthermore, the low amount of organic surfactant used was considered to be necessary to avoid the effect of them on gas sensing performance, in order to obtain good accessibility of the micronanostructure of the surface.

Besides their morphologies, the nonstoichiometry (i.e., crystal defect) on crystal surface is considered to be a key factor in determining properties of ZnO nanomaterials,[13,14] and the oxygen-related defects are proved to be linearly proportional to the gas sensing properties.[2,15,16] However, few studies are concerned about enhancing the gas-sensing properties by tuning the microstructure of ZnO nanomaterials. In addition, as the sensing materials usually need to be aged to get a better stability, there should be some defect redistributions on their surface due to the lattice creep and lattice reconstruction.[15,17] Neil indicated that, during the thermal activation, the low oxygen partial pressure of the system promotes oxygen anions (O^{2-}) to react and form oxygen molecules (O_2), and the formed oxygen molecules are then removed from the surface to create oxygen vacancies, which is critical to the activity of a catalyst.[15] Moreover, as the {10$\bar{1}$1} facet of the synthesized ZnO NPys is calculated to be more unstable than the {0001}

and the $\{10\bar{1}0\}$ facets;[7,11] in order to reduce its surface energy, there should be a large scale of nanoscopic defect reconstruction on it during the aging process, which leads to a significant effect on its sensing performance.[18] Thus, it is necessary to choose a proper aging condition to get a better sensing property. The aging temperature of the ZnO NPys cannot be set as high as those of other reports.[19,20] Moreover, in addition to the deep donor oxygen vacancy (V_O), zinc interstitial (Zn_i) as a shallow donor would have a competition with V_O to absorb more oxygen.[21] Additionally, due to their different formation energies,[22] the distribution of them on the $\{10\bar{1}1\}$ facet should also be quite different from the $\{0001\}$ and the $\{10\bar{1}0\}$ facets, which have not been studied earlier.

Thus, on the basis of anhydrously synthesizing ZnO NPys with uniform size and high crystallinity, the effect of aging temperature on sensing performance was studied in our work. In addition, the mechanisms of various sensing properties were discussed via the specific defect reconstruction of the $\{10\bar{1}1\}$ crystal facets, and a model of depletion layer changing was built.

2. EXPERIMENTAL SECTION

Dodecanol (DDL) was purchased from Tianjin Fuchen Chemical Reagents Factory. Oleylamine (OAM) was bought from Shanghai Aladdin Reagents. Zinc acetate dihydrate and the absolute ethanol used throughout the experiments were purchased from Beijing Chemical Works. All the chemicals above were of analytical grade and were used without further purification.

2.1. Synthesis of the ZnO NPys. The ZnO nanopyramids were synthesized via a solvothermal method as reported in previous work.[11] Briefly, 0.5 mol (0.2195 g) zinc acetate was dissolved in the mixed solution of 3 mL of OAM and 6 mL of DDL until a transparent solution was obtained. Then the obtained solution was heated to about 180 °C and kept for 2 h, and a milky white suspension appeared. After the reaction, the precipitate was filtered and rinsed with 75 °C absolute ethanol and cyclohexane several times and dried in the vacuum at 60 °C for 10 h.

2.2. Characterizations. The crystal phase and crystallinity of the synthesized ZnO NPys were recorded via X-ray diffraction (XRD) using Cu Kα radiation (λ = 0.154 06 nm) at a scanning rate of 10°/min in the range 20−90°. The IR spectra of the ZnO NPys were measured on a 370MCT Fourier transform infrared spectrometer in the range 400−4000 cm^{-1} at a resolution of 4 cm^{-1}. The morphologies of the products were observed on an S-4700 field emission scanning electron microscope (SEM) and a Tecnai G^{2}20 transmission electron microscope (TEM), and the high-resolution transmission electron microscope (HRTEM) and the selected area electron diffraction (SAED) patterns were recorded on a J-3010 microscope. The UV−vis diffuse reflectance spectra (UV−vis DRS) of the products were obtained by using a JMNU-3010 UV−vis spectrophotometer equipped with an integrated sphere reflectance accessory, and the baseline correction was done by using BaSO$_4$. The PL spectra were measured on a Hitachi Model F-7000 PL spectrophotometer at room temperature with the excitation wavelength of 325 nm. The Raman spectra were obtained on a Horiba Jobin Yvon Aramis spectrometer operating with an excitation wavelength of 532 nm. X-ray photoelectron spectroscopy was collected on a VG Scientific ESCALAB 250X using Al Kα excitation (calibrated C 1s = 248.4 eV), with the whole spectra resolution of 1.0 eV and the fine resolution of 0.5 eV.

2.3. Gas Sensing Test. The gas sensor chosen here is of the side-heated type. For the fabrication of a gas sensor, a proper amount of the ZnO NPys were ground in an agate mortar together with several drops of ethanol to form a sensing paste. Then, the paste was coated on the outer surface of an alumina ceramic tube attached with a pair of Au electrodes and four Pt wires and then dried in the air. To improve their thermal stability and repeatability, the sensors were aged for 24 h before test. Then, a piece of Ni−Cr alloy inserted through the inner tube was employed as a heater to control the operating temperature,

while allowing for the control of working temperature by adjusting the heating voltage. Figure 1 shows the schematic diagram of the sensor
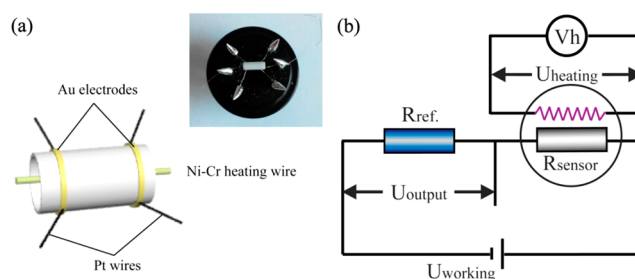

Figure 1. (a) Schematic diagram of the sensor. (b) Illustration of the measuring electric circuit.

and the measuring electric circuit. The sensitivities of the sensor toward test gases were measured on a WS-30A gas sensing test system (Winsen Electronics Technology Co. Ltd., Zhengzhou, China) at a relative humidity (RH) of 30 ± 10%, and the humidity did not show any significant effect on the sensing response. The gas sensitivity of the sensor, S_g, is defined as R_g/R_a, to oxidative gases, and R_a/R_g, to reductive gases, respectively, where R_g is the electrical resistance of the sensor in the presence of the analyzed gas and R_a is that in the air.

3. RESULTS AND DISCUSSION

3.1. Structural and Morphological Characterizations. Figure 2 shows the XRD patterns of the synthesized ZnO
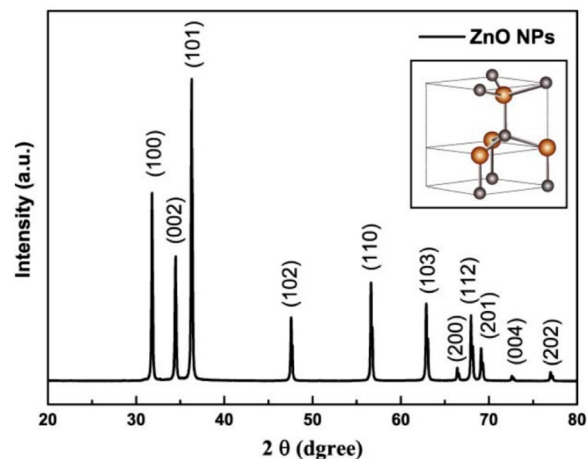
Figure 2. XRD patterns of the ZnO NPys with the illustration of the wurtzite structure.

NPys. All of the diffraction peaks can be well-indexed to the hexagonal wurtzite structure (shown in the inset of Figure 2). The calculated lattice constants a = 3.254 Å and c = 5.215 Å were consistent with the standard values of the JCPDS card no. 36-1451, which shows the good crystallinity of the products. The SEM image shown in Figure 3a with a 3D model of single pyramid (inset) reveals that the hexagonal pyramid-shaped ZnO nanocrystals were of uniform size with a basal edge length of ~100 nm and a height of ~200 nm. Figure 3b,c exhibits the corresponding TEM images of the ZnO nanopyramid. As labeled in Figure 3b, the angle between the opposite edges of the pyramid is 64°, while the angles between the edges and the basal plane are around 58°, which are consistent with the hexagonal pyramid structure.[7,10] Figure 3d shows the HRTEM image of the basal plane as red marked in Figure 3c, with a
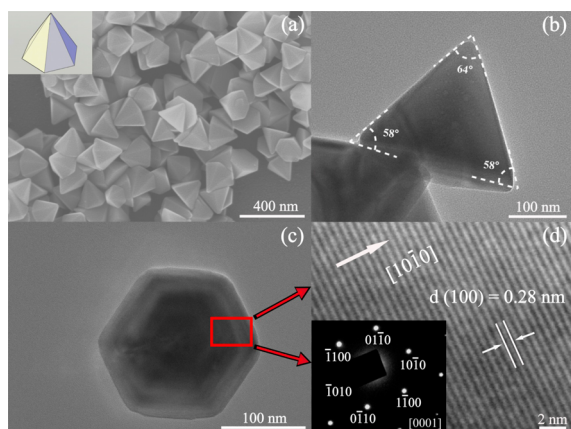
Figure 3. (a) SEM image of the synthesized ZnO NPys with a 3D structure model (inset). (b) TEM image of the ZnO NPys. (c) TEM image of the hexagonal basal plane of the ZnO nanopyramid. (d) HRTEM image of the red marked region and its corresponding SAED pattern.

lattice fringes of 0.28 nm, which corresponds to the distance between the (100) planes. The result indicates that the pyramid growth direction is along the [0001] axis, which is in agreement with the SAED pattern, as shown in the inset of Figure 3d. Thus, owing to the growth direction and the hexagonal pyramid structure, the exposed side surfaces of the ZnO NPys are identified as the $\{10\bar{1}1\}$ facets with the basal crystal plane of the $\{0001\}$ facet. Compared with the nonpolar crystal facets of

other ZnO nanorods and ZnO nanoflakes,[10,12] due to its large percentage content, the crystal plane $\{10\bar{1}1\}$ may probably be the dominant exposed facet of the ZnO NPys. Moreover, because the polar $\{10\bar{1}1\}$ plane seems to have the highest surface energy and usually grows too fast to be seen in the final shape of the crystal,[11,23] the surfactant OAM used here does not only serve as the capping agent but also reduces the surface energy of the $\{10\bar{1}1\}$ facet, resulting in a relatively slow growth rate and a stable exposed facets of the ZnO NPys.[23,24]

3.2. Gas Sensing Test of the ZnO NPys. Due to the particular $\{10\bar{1}1\}$ crystal facets exposing, the gas sensing performances of the as-prepared ZnO NPys were characterized in terms of the nonstoichiometric crystal defects on its surface. To avoid the morphological change and the agglomeration of the high temperature calcinates (Supporting Information Figure S1), the ZnO NPys aged at lower temperatures for 24 h were studied. Four different aging temperatures were chosen to study the effect of aging condition on their gas sensing properties: the product synthesis temperature 180 °C, the usual sensing temperature 250 °C, the general aging temperature 300 °C, and a higher aging temperature 400 °C, with their products being denoted as ZnO180, ZnO250, ZnO300, and ZnO400, respectively.

The sensing properties to 100 ppm ethanol of the ZnO NPys aged at different temperatures were evaluated by determining the optimum operation temperature as shown in Figure 4a. As we can see, the gas responses of all the sensors enhanced with the temperature increasing in the range 195−225 °C, and reduced when the temperature was above 225 °C. They showed a maximum response at the low temperature of 225 °C.
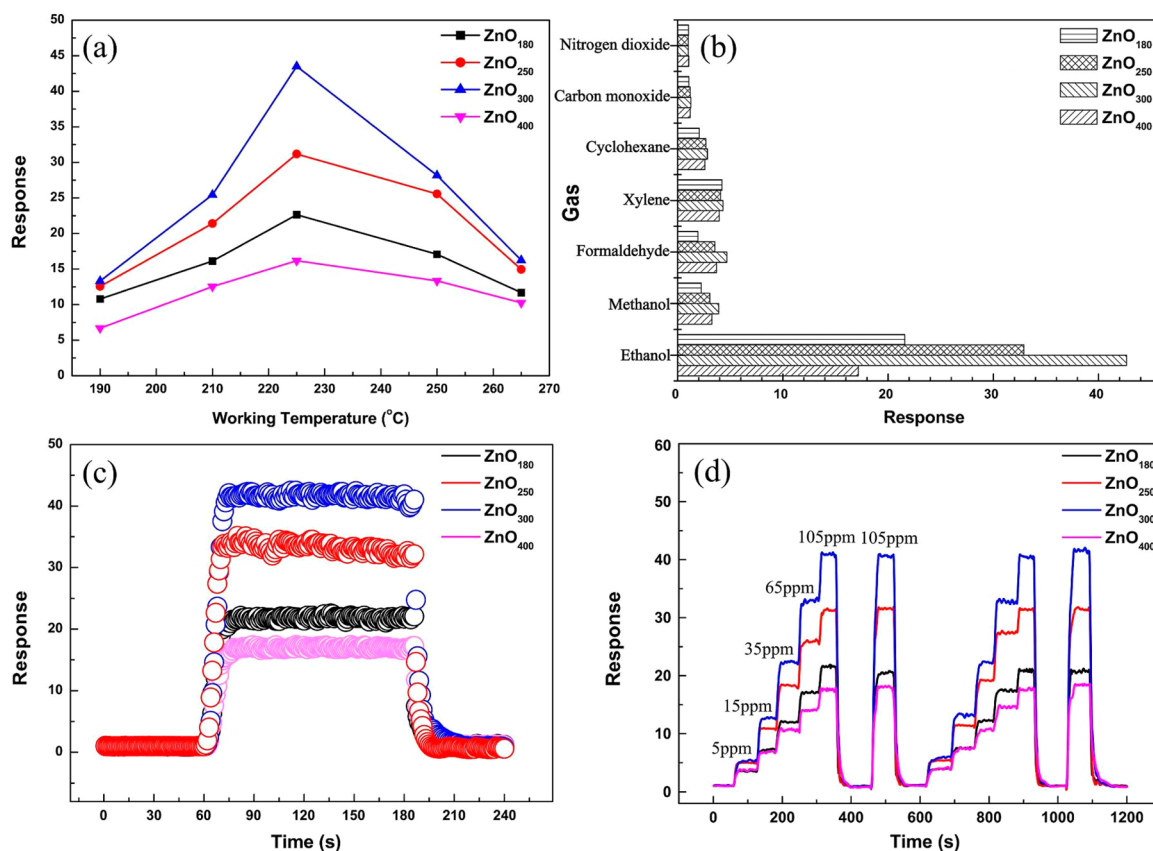
Figure 4. (a) Responses of the ZnO NPys to 100 ppm ethanol versus operating temperature. (b) Sensitivities of the ZnO NPys to 100 ppm toxic gases and 100 ppb NO_2 under the optimum working temperature of 225 °C. (c) Gas response-recovery curves of the ZnO NPys. (d) Continuous response-recovery curves of the ZnO NPys to ethanol at different concentrations.

Table 1. Comparing with Ethanol Responses of ZnO Sensors Obtained in Prior Reports

structure	ethanol concentration	working temperature	response	res/rec time	refs
ZnO nanopyramids	100 ppm	225 °C	43.2	11/8 s	present work
ZnO nanoflakes	100 ppm	320 °C	24.3	3/15 s	6
ZnO nanopyramids	300 ppm	350 °C	9.3		10
ZnO nanopyramids	250 ppm	260 °C	5.72	8/48 s	27
ZnO nanorod arrays	100 ppm	230 °C	20		28
ZnO nanorods	100 ppm	320 °C	26	60/50 s	30
ZnO nanoflowers	100 ppm	300 °C	33.1	2/20 s	31
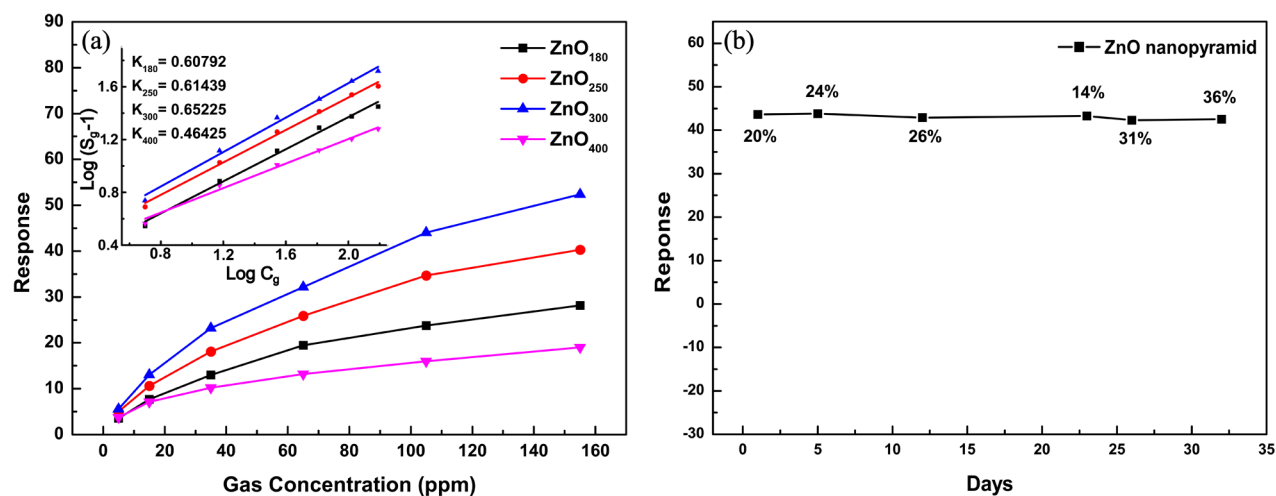
Figure 5. (a) Gas responses of the aged ZnO NPys as a function of ethanol concentration at 225 °C with their corresponding $\log(S_g - 1)$ versus $\log C_g$ curves (inset). (b) Sensing stability of the ZnO_{300} for nearly one month.

That was because, at low temperatures, the absorbed ethanol molecules are not sufficiently activated to conquer the energy barrier to react with the absorbed oxygen. Nonetheless, at the temperatures higher than the optimum, the stably absorbed ethanol molecules begin to desorb in a large quantity, which causes a low gas response.[25] Comparing the gas responses of the different sensors, it can be easily concluded that the ZnO_{300} has the highest sensitivity to 100 ppm ethanol with the response of approximately 45. The result indicates that, among different aging temperatures, 300 °C may be the best aging temperature, which is quite different from other reports.[26,27] In addition, in contrast to the sensing results of those high temperature calcinates as shown in Supporting Information Figure S2, it can be obviously concluded that the morphological changing and agglomeration have an enormous effect on their sensing properties. Thus, for the synthesized ZnO NPys, the lower temperature aging is more preferable for the surface defect engineering. Figure 4b exhibits the selectivity of the gas sensor to various toxic gases; all of the sensors show a preferable response to ethanol as compared to other reductive gases and exhibit almost no sensitivity to the oxidative gas of NO_2. The result illustrates that, compared with other reports,[26−28] the synthesized ZnO NPys can be a good candidate for ethanol detecting due to its superior selectivity to ethanol.

Figure 4c demonstrates the curves of response-recovery time measured at the optimum working temperature, wherein the response time is defined as the time taken to reach 90% of the total resistance change after the detected gas was injected, and the recovery time is defined as the time taken to return to 10% of the total resistance change after the detected gas was removed. It can be concluded that, as the aging temperature

increases, the response times of ZnO_{180}, ZnO_{250}, ZnO_{300}, and ZnO_{400} were calculated to be 12, 10, 10, and 15 s, respectively, while the recovery times were calculated to be 15, 9, 9, and 8 s, respectively. The result shows that the ZnO_{300} has a shorter response-recovery time than the others, which may be attributed to the greater number of donor defects in crystal. These defects make the nanostructure unstable and able to react with O_2 or reducing gases; hence, a fast absorption−desorption process was obtained.[29] The continuous response-recovery curves of the sensors upon exposure to ethanol at different concentrations are shown in Figure 4d. It can be observed that the response largely depends on the ethanol concentration, and all of the sensors show good reversibility to return to the base resistance with fast recovery rate. In conclusion, the fast response-recovery time, the lower working temperature, the higher gas response, and the prominent selectivity all suggest that thanks to its high crystallinity, uniform subsize, and particular facet exposing of $\{10\bar{1}1\}$, the ZnO NPys will be an ideal candidate for ethanol detecting. Further, compared with other works reported earlier, the ZnO NPys exhibit a much better gas response to ethanol, as shown in Table 1.

Figure 5a exhibits the corresponding responses of the aged ZnO NPys to ethanol in the concentration range 5−155 ppm. It is apparent that the responses of the sensors improve with the gas concentration increasing, and the growth slows down gradually. The results are consistent with other materials.[25,30] Furthermore, the real response of the sensor at the concentration of 5 ppm also confirms that the detection limits of the sensing should be even less. Then, the response data were processed via a double logarithmic treatment, in order to make them be consistent with the gas absorption model of

semiconductors. The gas absorption on the surface of a semiconducting-oxide-based sensor can be described empirically as[32]

$$S_g = 1 + aC_g^b \qquad (1)$$

where S_g is the sensitivity, C_g is the concentration of the test gas, and a and b are constants depending on the electrical charge of the surface species and the stoichiometry of the elementary reactions on the surface. It is reported that when b is 0.5, the adsorbed surface oxygen ion is O^{2-}, while it changes into O^- when b is 1.[32,33] Thus, if the value of b is calculated, the oxygen ion species adsorbed on the surface of the ZnO NPys can be deduced. Equation 1 can be rewritten as

$$\log(S_g - 1) = a + b \log C_g \qquad (2)$$

From eq 2, it can be seen that $\log(S_g - 1)$ has a linear relation with $\log C_g$, with b being the slope value, which can be easily obtained from the slope of a $\log(S_g - 1) \sim \log C_g$ curve (inset of Figure 5a). As can be observed from Figure 5a (inset), there is a good linear relation between the logarithm of the sensitivity and the logarithm of the concentration for all the sensors. Furthermore, the b values are all relatively close to 0.5, which implies that the oxygen species absorbed on the ZnO NPys is almost O^{2-}. As the adsorbed O^{2-} species is much more unstable and energetic than others (O_2, O_2^-, and O^-), the large quantity of the adsorbed O^{2-} may account for the high response of the as-prepared ZnO NPys.[33] For the ZnO_{300}, as its b value is the largest, it shows the best sensing property. Figure 5b shows the stability result of the ZnO_{300} to 100 ppm ethanol, with the test humidity remarked above. It can be speculated that humidity is not the overwhelming influence factor of the sensing performance. The sensor exhibited nearly a constant response during 30 days, confirming the good stability of the aged ZnO NPys.

3.3. Surface Characterizations of the ZnO NPys. As we all know, the sensing mechanism of ZnO gas sensor can be recognized as being surface-controlled. It is the content of adsorbed oxygen that determines its gas response, which is closely in proportion to the surface defects of the sensor.[22-24] The crystal defects of ZnO nanomaterials can be classified into two element species, wherein zinc interstitial (Zn_i), zinc vacancy (V_{Zn}), and zinc antisite (Zn_O) belong to zinc defects, and oxygen interstitial (O_i), oxygen vacancy (V_O), and oxygen antisite (O_{Zn}) belong to oxygen defects. The Zn_O is considered to be unstable and needs high energy to be produced, even in a Zn-rich atmosphere, and thus is ruled out in common studies.[34] Among the left five types, Zn_i and V_O give rise to free electrons in ZnO crystal, acting as electron donors, while V_{Zn}, O_i, and O_{Zn} consume free electrons, playing an opposite role. By contrast, it can be considered that these donor defects will act as active sites for the chemisorption of the atmospheric oxygen during gas sensing, and make the reaction go forward in the positive direction, while the acceptor defects act oppositely.[14,33] Hence, for a reasonable explanation on the various sensing properties, characterizations of the surface structures were used to get a deeper understanding of the intrinsic defects.

The TEM images of the products aged at different temperatures are shown in Figure 6a−d. It is apparent that, at the higher aging temperature of 400 °C, the apexes of the pyramids become smooth with large morphological change, while at lower temperatures the features can maintain well. Therefore, it can be confirmed that the aging temperature has a
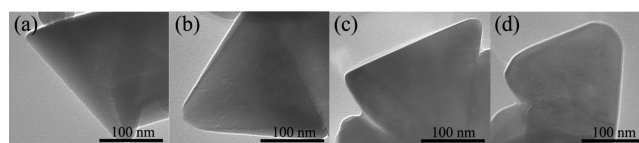
Figure 6. TEM images of the ZnO NPys aged at different temperatures for 24 h: (a) ZnO_{180}, (b) ZnO_{250}, (c) ZnO_{300}, (d) ZnO_{400}.

significant effect on the gas sensing properties of the ZnO NPys. The high-temperature calcination would lead to a crystal deformation in the form of defect and atom reconstruction, which causes a negative effect on the sensing performance. Compared with the TEM and SEM images of the ZnO NPys after gas sensing test (Supporting Information Figure S3), the products maintained the morphology well, which also demonstrates the good stability of the ZnO NPys. In addition, similar to the IR results of the high temperature calcinates (Supporting Information Figure S4a), the IR spectra of the different aged products are shown in Supporting Information Figure S4b, with several peaks lying in the range 400−4000 cm^{-1}. To be more specific, the bands at 3420, 1630, and 1350 cm^{-1} are assigned to the stretching vibration and bending vibration of the absorbed water on the surface. The band at 2359 cm^{-1} is correlated to the carbon dioxide, while the band at 500 cm^{-1} corresponds to the typical E_2 mode of the hexagonal ZnO.[35] No other peaks are found, confirming that, after being aged at the lower temperature of 180 °C for 24 h, the surfactant molecules adsorbed on ZnO surface were completely removed and had no effect on sensing properties.

UV−vis diffuse reflectance spectroscopy was used to study the band gap and the electron states of the aged ZnO NPys, as shown in Supporting Information Figure S5. It can be observed that all of the products have a strong adsorption around 390 nm in the UV region, corresponding to the band to band transition.[36,37] As a direct-band semiconductor, the relation between the absorption coefficient (α) and the incident photon energy ($h\upsilon$) of ZnO nanomaterial can be written as[38]

$$\alpha h\upsilon = C(h\upsilon - Eg)^{1/2} \qquad (3)$$

where C is a constant and E_g is the band gap. By extrapolating the linear portion of the $(h\upsilon) \sim (\alpha h\upsilon)^2$ plot to $(\alpha h\upsilon)^2 = 0$, the band gap energy may be equal to the horizontal intercept of the x axis, as shown in Supporting Information Figure S6. It can be concluded that the product aged at 300 °C has the smallest band gap of 3.28 eV, while the E_g values for ZnO_{180}, ZnO_{250}, and ZnO_{400} are 3.30, 3.29, and 3.32 eV, respectively. The smaller the E_g is, the less energy the electron needs for transition. Thus, there may be more free electrons on the ZnO_{300} surface, which can attract more adsorbed oxygen species. Moreover, the decrease in the band gap value also confirms the presence of more oxygen vacancies, which indicates that the ZnO_{300} may have the most electron donors, leading to a better sensing property than the others.[39] Furthermore, the negligible differences between the products can also reveal that there is not severe morphology changing but the microcosmic changing in the form of defect redistribution on their surfaces.

As it is well-established that the luminescence of ZnO nanomaterial originates from the photoinduced electron−hole combinations or the intrinsic defects,[34,38] the PL characterization was used to determine the specific percentage of each

312

dx.doi.org/10.1021/am506206c | ACS Appl. Mater. Interfaces 2015, 7, 308−317

intrinsic defect in the ZnO NPys. As shown in Supporting Information Figure S7, according to their originations, the whole PL spectrum in the range 360−600 nm can be Gaussian deconvoluted into seven parts.[40,41] The sharp ultraviolet (UV) peak at ~375 nm is attributed to the exciton emission from conduction band to valence band (CB−VB combination). The UV emission peaks at ~395 and 420 nm can be indexed to the shallow donor Zn_i. The peak at ~460 nm is associated with V_{Zn}. The peak at ~490 nm is attributed to V_O. The peak at ~520 nm is related to O_{Zn}, while the origins of yellow and orange luminescence above 540 nm are attributed to O_i. The compositions of these defects are summarized in Table 2. It

Table 2. Summarized Percentages of the PL Spectra Deconvoluted by Gaussian Distribution

origination	peak (nm)	ZnO₁₈₀	ZnO₂₅₀	ZnO₃₀₀	ZnO₄₀₀
(CB-VB) combination	375	29.28	30.15	34.39	22.33
Zn_i (3.30−3.40 eV)	395	23.52	28.60	28.08	18.85
Zn_i (~2.90 eV)	420	19.15	15.69	17.21	20.84
V_{Zn} (~2.70 eV)	460	9.51	7.99	10.89	15.92
V_O (~2.53 eV)	490	5.18	5.47	6.30	8.38
O_{Zn} (~2.38 eV)	520	8.41	8.75	2.10	8.36
O_i (~2.23 eV)	540	4.95	3.35	1.03	5.32
DL ($Zn_i + V_O$)		47.85	49.76	51.59	48.07
AL ($V_{Zn} + O_{Zn} + O_i$)		22.87	20.09	14.02	29.60

can be suggested that since the content of the electron donors of the ZnO NPys is higher than that of ZnO nanoparticles (19.1%),[34] (35.5%),[40] and nanorods (39.77%),[42] the ZnO NPys exhibited a much higher response to ethanol. In addition to V_O, the Zn_i is the dominant defect on the $\{10\bar{1}1\}$ crystal facet of the ZnO NPys, which is different from other materials.[38,42] Furthermore, by a deep comparison, the electron donors (DL) increase and the electron acceptors (AL) decrease in the temperature range 180−300 °C, which indicates that the product ZnO₃₀₀ has the most DL and the least AL. Thus, it can provide more electrons to the redox reaction of the absorbed ethanol molecules, which contributes to the best response. For the ZnO₄₀₀, though its content of DL is higher than that of the ZnO₁₈₀, it is the more AL that leads to the lowest response. In addition, it can be summarized that the content of the V_O increases with the aging temperature rising, which implies that the higher temperature is more beneficial for the formation of V_O.

Furthermore, Raman spectra were also used to characterize the density and type of the defects of the ZnO NPys, as it is a versatile technique for defect detecting.[43,44] The spectra of the different aged products are shown in Figure 7. The most intense peak located at ~437 cm⁻¹ is attributed to the vibration mode E_{2H} from oxygen atom.[9,45] The strong peak at this position is the characteristic of the wurtzite crystal structure, indicating that the samples have a perfect crystallinity.[46] The other peaks centered at ~330 and ~380 cm⁻¹ are assigned to the modes $E_{2H}-E_{2L}$ and A_{1T} of the ZnO crystal, respectively.[38,47] Besides these peaks, a small peak located at ~583 cm⁻¹ is correlated to the vibration mode E_{1L}, which is usually demonstrated to be caused by the donor defects, such as V_O and Zn_i.[48−50] As shown in Figure 7, it can be observed that among the different aged samples, the ZnO₃₀₀ exhibits the strongest peak at ~583 cm⁻¹, which implies that the ZnO₃₀₀ will have the most electron donors and the ZnO₁₈₀ has the
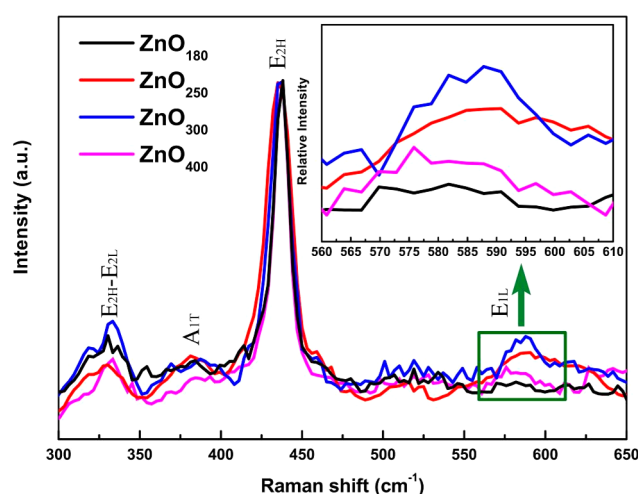
Figure 7. Raman spectra of the different aged products.

least. Additionally, the result is in agreement with the PL characterizations.

XPS spectra were carried out to determine the non-stoichiometric detects and the content of the oxygen species of the ZnO NPys. As shown in Supporting Information Figure S8, the whole spectra are composed of Zn, O, and a small amount of adventitious carbon C 1s originated from the conducting resin, indicating that all of the products are pure ZnO and on organic components exist. Supporting Information Figure S9 shows the Gaussian decomposition spectra of the Zn and O species. According to their originations, the Zn_{LMM} Auger electron spectra (AES) can be classified into two Gaussian parts, wherein one is the main peak at ~495 eV, attributing to the Zn_i, and the other is the subpeak at ~498 eV, representing the lattice zinc (Zn^{2+}).[51] The specific percentages of these Zn species are shown in Table 3. It can be found that

Table 3. Comparison of the Zinc Species and the Oxygen Species between the ZnO NPys Aged at Different Temperatures

species	peak (nm)	ZnO₁₈₀	ZnO₂₅₀	ZnO₃₀₀	ZnO₄₀₀
Zn_i	495	40.44	41.58	44.44	39.76
Zn^{2+}	498	59.56	58.42	55.56	60.24
O_I	530.0	54.94	53.03	47.12	45.24
O_{II}	531.4	19.98	21.28	23.84	33.04
O_{III}	533.0	25.08	25.69	29.04	21.72

the content of the Zn_i is the highest in the ZnO₃₀₀ and lower in the ZnO₄₀₀. Also, as Zn_i is the defect that is helpful for gas sensing, the result is in consistent with the gas sensing tests. Moreover, according to the change of bonding energy, the O 1s core level in the range 527−536 eV can be fitted with three Gaussians, centering at 530.0 ± 0.15 eV (O_I), 531.4 ± 0.15 eV (O_{II}), and 533.0 ± 0.15 eV (O_{III}), respectively.[34,41] The low bonding energy peak (O_I) centered at ~530.0 eV is usually ascribed to the lattice oxygen in the hexagonal wurtzite structure, and its intensity is proportional to the amount of the oxygen in a fully oxidized stoichiometric surrounding.[41,52,53] The medium peak (O_{II}) located at ~531.4 eV is associated with the O^{2-} ions in the oxygen deficient regions within the matrix of ZnO.[44,51,54] The high bonding energy peak (O_{III}) situated at ~533.0 eV is attributed to the chemisorbed or dissociated oxygen or OH species on the material surface, such as absorbed
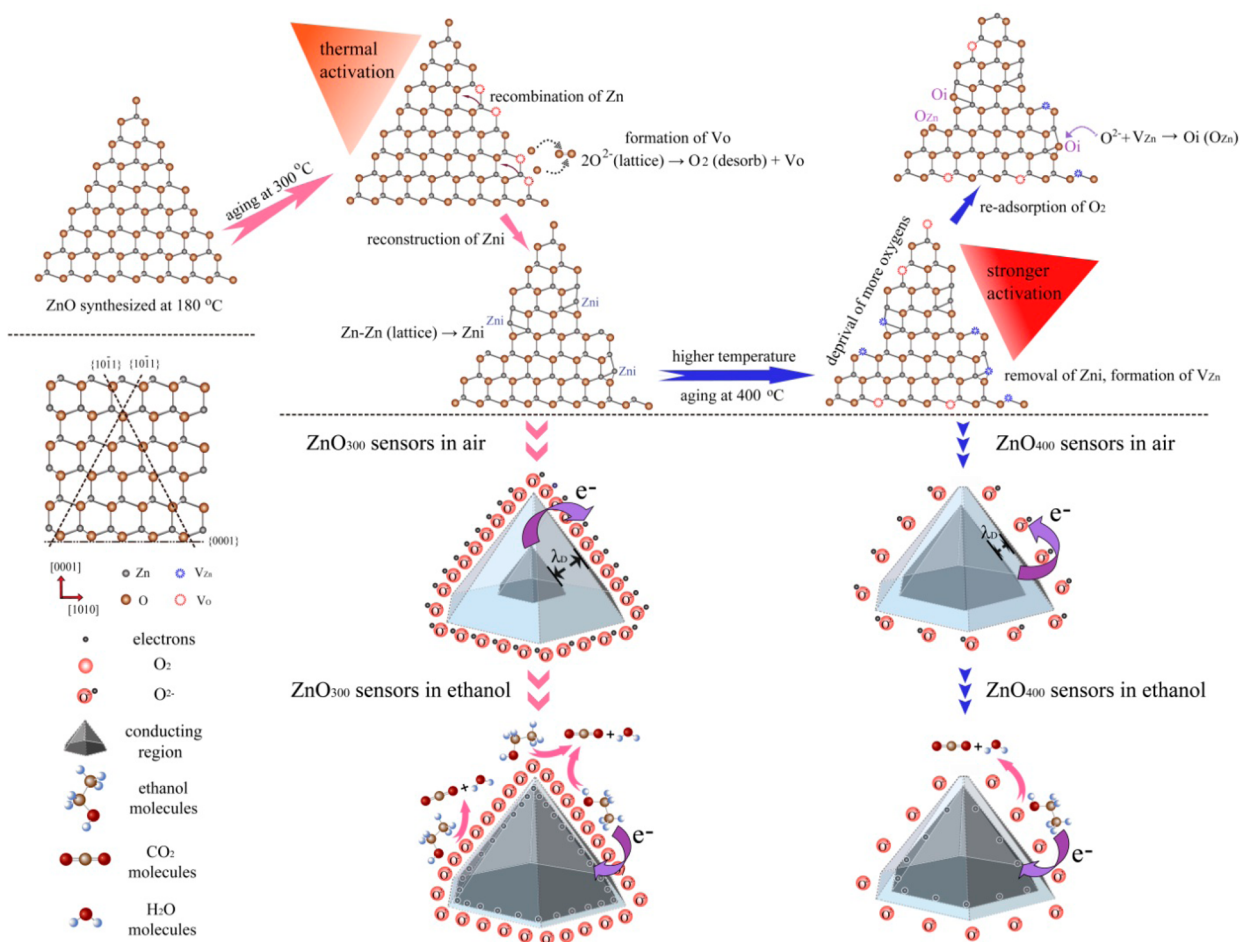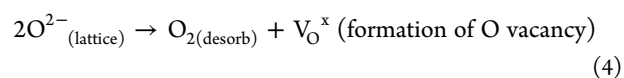
Figure 8. Defect redistribution of the ZnO NPys aged at different temperatures and the illustrations of their sensing processes via the depletion layer changing in air and in ethanol (the blue region is the depletion layer (λ_D), the gray region is the conducting area, and the O^{2-} means the absorbed oxygen).
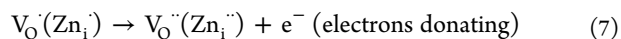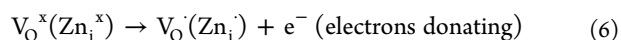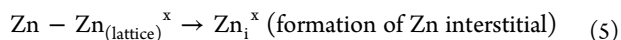
O_2 and H_2O.[51,55,56] The compositions of these oxygen species are shown in Table 3. It can be found that the ZnO_{300} has the most Zn_i and the most O_{III}, which can react with more ethanol molecules, leading to the best gas response. However, the ZnO_{400} has the lowest O_{III}, which can be attributed to the existence of other electron acceptors or the larger morphological changing.

3.4. Proposed Mechanism. From the above, it can be concluded that, in addition to V_O, the sensing performance of the ZnO NPys is decided by the combined effect of V_O and Zn_i, with all of the defects redistributed on the surface. The ZnO_{300} exhibits the best gas response, owing to greater DL, which can absorb a larger amount of oxygen to react with more ethanol molecules. For the ZnO_{400}, though it has the largest content of V_O, it is the greater percentage of AL accompanied by the defect reconstruction and morphological changing that leads to its worst sensing property. Thus, models of defect redistribution and depletion layer changing are used to intuitively exhibit the sensing mechanisms of different products.
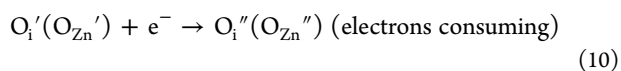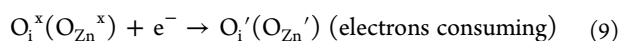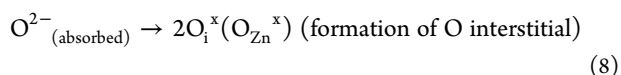
For a typical illustration, only the representative products ZnO_{300} and ZnO_{400} are chosen to exhibit the defect redistribution of the $\{10\bar{1}1\}$ facets, as shown in Figure 8 (because the ZnO_{250} has the same tendency with the ZnO_{300}, it will not be discussed again). To get a more obvious procedure of defect redistribution, we presume that the ZnO NPys synthesized at 180 °C are completely grown as the perfectly

stoichiometric pattern with no defect existing on the surface. As can be seen from Figure 8, the ZnO nanopyramid is composed of the $\{10\bar{1}1\}$ and the $\{0001\}$ crystal facets, both of which are alternately arranged by oxygen and zinc atoms. Because the $\{0001\}$ facet was more stable than the $\{10\bar{1}1\}$ facet as calculated, it will not be discussed as the main body of the defect reconstruction. Hence, on account of the highly energetic characteristic of the $\{10\bar{1}1\}$ facet, part of the oxygen anions (O^{2-}) will react and form oxygen molecules (O_2) when the material was thermally activated at 300 °C. Then the formed oxygen molecules will be removed from the surface to produce much V_O and nonbonding zinc atoms, which reduces the surface energy of the $\{10\bar{1}1\}$ facet.[15,57] Then, because there is much interspace in the ZnO tetrahedron and the zinc ion has a smaller radius than the oxygen ion, the nonbonding zinc atoms which lose their bonding oxygen atoms may have enough space to travel. Next, these active Zn atoms nearby will have an interaction and recombine into the Zn_i (Zn−Zn bond) to stabilize the crystal energy, for the formation energy of Zn_i is much lower than the other defects.[58,59] In addition, owing to its low diffusion, the Zn_i is preferable to move to the surface and act as electron donor to provide electrons to absorb more oxygen.[59,60] The electronic transfer can be described as follows:

$$2O^{2-}_{(lattice)} \rightarrow O_{2(desorb)} + V_O^x \text{ (formation of O vacancy)}$$

$$(4)$$

314

dx.doi.org/10.1021/am506206c | *ACS Appl. Mater. Interfaces* 2015, 7, 308−317

$$Zn - Zn_{(lattice)}{}^x \rightarrow Zn_i{}^x \text{ (formation of Zn interstitial)} \quad (5)$$

$$V_O{}^x(Zn_i{}^x) \rightarrow V_O{}^{\cdot}(Zn_i{}^{\cdot}) + e^- \text{ (electrons donating)} \quad (6)$$

$$V_O{}^{\cdot}(Zn_i{}^{\cdot}) \rightarrow V_O{}^{\cdot\cdot}(Zn_i{}^{\cdot\cdot}) + e^- \text{ (electrons donating)} \quad (7)$$

However, when the temperature increased to 400 °C, the higher temperature induced the stronger activation. More oxygen atoms were removed, along with the loss of some zinc atoms, resulting in the increasing of the V_O and V_{Zn} and the reduction of the Zn_i. Moreover, the released oxygen may incorporate into the ZnO lattice again and react with the nonbonding oxygen atoms to produce O_i and O_{Zn}.[34,41] Then the formed O_i and O_{Zn} will act as the electron acceptors which consume the electrons, and introduce an adverse effect on the sensing performance as shown in eqs 8, 9, and 10:

$$O^{2-}{}_{(absorbed)} \rightarrow 2O_i{}^x(O_{Zn}{}^x) \text{ (formation of O interstitial)} \quad (8)$$

$$O_i{}^x(O_{Zn}{}^x) + e^- \rightarrow O_i{}'(O_{Zn}{}') \text{ (electrons consuming)} \quad (9)$$

$$O_i{}'(O_{Zn}{}') + e^- \rightarrow O_i{}''(O_{Zn}{}'') \text{ (electrons consuming)} \quad (10)$$

Thus, owing to the large amount of surface atoms losing and electron acceptors producing, the ZnO_{400} changed its morphology and reduced its crystallinity, which results in the worst sensing property.

Furthermore, as it is the number of free electrons on the surface that determines the sensing performance of ZnO nanomaterial,[38,51] the response process of the ZnO NPys with different depletion thicknesses (λ_D) are shown in Figure 8. The λ_D of the sensor is thought to be proportional to the density and mobility of the free electrons on the surface.[27,33] When the sensor is exposed to air, oxygen molecules are adsorbed on the surface and form the oxygen ions by extracting electrons from the conduction band, such as $O_2{}^-$, O^-, and O^{2-} (where for the ZnO NPys, the O^{2-} should be the dominant species, as discussed above). The electron loss of the conduction band results in a thick depletion region with high potential barrier, which can be described as eqs 11, 12, and 13:[38,61]

$$O_{2(air)} + e^- \rightarrow O_{2(ads)}{}^- \quad (11)$$

$$O_{2(ads)}{}^- + e^- \rightarrow 2O_{(ads)}{}^- \quad (12)$$

$$2O_{(ads)}{}^- + e^- \rightarrow O_{(ads)}{}^{2-} \quad (13)$$

The more electron donors exist, the thicker the depletion layer will be. That indicates that the product ZnO_{300} should have the largest λ_D, as shown in Figure 8. In contrast, once the sensor exposes to ethanol, the reductive gas will react with the adsorbed oxygen ions and return the electrons into the conduction region. The carrier concentration becomes higher and the depletion layer gets thinner, leading to a decreasing of the electrical resistance of the sensor, as can be expressed by the following reaction:

$$CH_3CH_2OH_{(ads)} + 6O_{(ads)}{}^{2-} \rightarrow 2CO_2 + 3H_2O + 12e^- \quad (14)$$
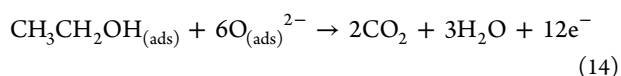
Thus, it can be observed that, due to its high content of the absorbed O^{2-} species and the absorbed ethanol molecules, the ZnO_{300} exhibits the biggest change of λ_D, resulting in the highest gas response. Nevertheless, for the ZnO_{400}, thanks to its high content of the electron acceptors, the free electrons are

partly consumed by these defects, leading to a thinner λ_D, and less absorbed ethanol molecules release electrons. Hence, the ZnO_{400} shows the smallest change of the depletion layer, which will be responsible for the worst sensing performance.

4. CONCLUSION

In this work, the uniform ZnO nanopyramids with exposed crystal facets of $\{10\bar{1}1\}$ have been synthesized via a one-step solvothermal synthesis method using oleylamine as surface modifier. The gas sensing performances of the ZnO NPys have been improved via the surface defect engineering. At the aging temperature of 300 °C, the ZnO_{300} exhibits the best gas response with the fast response-recovery time and the excellent selectivity. It is observed that in addition to V_O, the gas sensing performance of the ZnO NPys is determined by the combined effect of V_O and Zn_i, with all of the defects redistributed on the surface. Models of defect redistribution and depletion layer changing are used to explicate the different sensing performances of the aged ZnO NPys. The highest response of the ZnO_{300} is attributed to its larger content of the electron donors (V_O and Zn_i) and more active oxygen molecules absorbed on the surface, while the ZnO_{400} exhibits an opposite feature. Some in situ characterizations are being conducted in our laboratory to get a much more detailed sensing mechanism of the ZnO NPys.

■ ASSOCIATED CONTENT

⑤ Supporting Information
TEM images and gas sensing results of the ZnO NPys that are calcinated at higher temperatures for 2 h (Figures S1 and S2); TEM and SEM images of the ZnO NPys after gas sensing test (Figure S3); FTIR spectra of the ZnO NPys (Figure S4); UV−vis, PL, and XPS spectra of the ZnO NPys that are aged at different lower temperatures for 24 h (Figures S5, S6, S7, S8, and S9). This material is available free of charge via the Internet at http://pubs.acs.org.

■ AUTHOR INFORMATION

Corresponding Author
*E-mail: gufb@mail.buct.edu.cn. Phone: +861064445927.
Notes
The authors declare no competing financial interest.

■ REFERENCES

(1) Kumar, R.; Anandan, S.; Hembram, K.; Narasinga Rao, T. Efficient ZnO-Based Visible-Light-Driven Photocatalyst for Antibacterial Applications. *ACS Appl. Mater. Interfaces* **2014**, *6*, 13138−13148.

(2) Gurav, K. V.; Gang, M. G.; Shin, S. W.; Patil, U. M.; Deshmukh, P. R.; Agawane, G. L.; Suryawanshi, M. P.; Pawar, S. M.; Patil, P. S.; Lokhande, C. D.; Kim, J. H. Gas Sensing Properties of Hydrothermally Grown ZnO Nanorods with Different Aspect Ratios. *Sens. Actuators, B* **2014**, *190*, 439−445.

(3) Talwar, V.; Singh, O.; Singh, R. C. ZnO Assisted Polyaniline Nanofibers and Its Application as Ammonia Gas Sensor. *Sens. Actuators, B* **2014**, *191*, 276−282.

(4) Su, D. W.; Fu, H. T.; Jiang, X. C.; Wang, G. X. ZnO Nanocrystals with A High Percentage of Exposed $\{4\bar{2}\bar{2}3\}$ Reactive Facets for

Enhanced Gas Sensing Performance. *Sens. Actuators, B* **2013**, *186*, 286−292.

(5) Hassan, J. J.; Mahdi, M. A.; Chin, C. W.; Abu-Hassan, H.; Hassan, Z. A High-Sensitivity Room-Temperature Hydrogen Gas Sensor Based on Oblique and Vertical ZnO Nanorod Arrays. *Sens. Actuators, B* **2013**, *176*, 360−367.

(6) Huang, J. R.; Wu, Y. J.; Gu, C. P.; Zhai, M. H.; Sun, Y. F.; Liu, J. H. Fabrication and Gas-Sensing Properties of Hierarchically Porous ZnO Architectures. *Sens. Actuators, B* **2011**, *155*, 126−133.

(7) Chang, J.; Ahmed, R.; Wang, H. D.; Liu, H. W.; Lo, R. Z.; Wang, P.; Waclawikt, E. R. ZnO Nanocones with High-Index {10$\bar{1}$1} Facets for Enhanced Energy Conversion Efficiency of Dye-Sensitized Solar Cells. *J. Phys. Chem. C* **2013**, *117*, 13836−13844.

(8) Herring, N. P.; AbouZeid, K.; Mohamed, M. B.; Pinsk, J.; El-Shall, M. S. Formation Mechanisms of Gold-Zinc Oxide Hexagonal Nanopyramids by Heterogeneous Nucleation using Microwave Synthesis. *Langmuir* **2011**, *27*, 15146−15154.

(9) Herring, N. P.; Panchakarla, L. S.; El-Shall, M. S. P-Type Nitrogen-Doped ZnO Nanostructures with Controlled Shape and Doping Level by Facile Microwave Synthesis. *Langmuir* **2014**, *30*, 2230−2240.

(10) Han, X. G.; He, H. Z.; Kuang, Q.; Zhou, X.; Zhang, X. H.; Xu, T.; Xie, Z. X.; Zheng, L. S. Controlling Morphologies and Tuning the Related Properties of Nano/Microstructured ZnO Crystallites. *J. Phys. Chem. C* **2009**, *113*, 584−589.

(11) Li, P.; Wang, D. S.; Wei, Z.; Peng, Q.; Li, Y. D. Systematic Synthesis of ZnO Nanostructures. *Chem.—Eur. J.* **2013**, *19*, 3735−3740.

(12) Joo, J.; Kwon, S. G.; Yu, J. H.; Hyeon, T. Synthesis of ZnO Nanocrystals with Cone, Hexagonal Cone, and Rod Shapes via Non-Hydrolytic Ester Elimination Sol-Gel Reactions. *Adv. Mater.* **2005**, *17*, 1873−1877.

(13) Chang, C. M.; Hon, M. H.; Leu, I. C. Preparation of ZnO Nanorod Arrays with Tailored Defect-Related Characteristics and Their Effect on the Ethanol Gas Sensing Performance. *Sens. Actuators, B* **2010**, *151*, 15−20.

(14) Ahn, M. W.; Park, K. S.; Heo, J. H.; Park, J. G.; Kim, D. W.; Choi, K. J.; Lee, J. H.; Hong, S. H. Gas Sensing Properties of Defect-Controlled ZnO-Nanowire Gas Sensor. *Appl. Phys. Lett.* **2008**, *93*, 263103.

(15) Lawrence, N. J.; Brewer, J. R.; Wang, L.; Wu, T. S.; Wells-Kingsbury, J.; Ihrig, M. M.; Wang, G. H.; Soo, Y. L.; Mei, W. N.; Cheung, C. L. Defect Engineering in Cubic Cerium Oxide Nanostructures for Catalytic Oxidation. *Nano Lett.* **2011**, *11*, 2666−2671.

(16) Fouad, O. A.; Glaspell, G.; El-Shall, M. S. Structural, Optical and Gas Sensing Properties of ZnO, SnO$_2$ and ZTO Nanostructures. *Nano* **2010**, *5*, 185−194.

(17) Chen, B.; Hu, J. N.; Flewitt, P. E. J.; Smith, D. J.; Cocks, A. C. F.; Zhang, S. Y. Quantifying Internal Stress and Internal Resistance Associated with Thermal Ageing and Creep in A Polycrystalline Material. *Acta Mater.* **2014**, *67*, 207−219.

(18) Norenberg, H.; Harding, J. H. The Surface Structure of CeO$_2$ (001) Single Crystals Studied by Elevated Temperature STM. *Surf. Sci.* **2001**, *477*, 17−24.

(19) Bai, S. L.; Sun, C. Z.; Guo, T.; Luo, R. X.; Lin, Y.; Chen, A. F.; Sun, L. N.; Zhang, J. B. Low Temperature Electrochemical Deposition of Nanoporous ZnO Thin Films as Novel NO$_2$ Sensors. *Electrochim. Acta* **2013**, *90*, 530−534.

(20) Bai, Z. K.; Xie, C. S.; Hu, M. L.; Zhang, S. P.; Zeng, D. W. Effect of Humidity on the Gas Sensing Property of the Tetrapod-Shaped ZnO Nanopowder Sensor. *Mater. Sci. Eng., B* **2008**, *149*, 12−17.

(21) Kim, S.; Park, H.; Nam, G.; Yoon, H.; Kim, J. S.; Son, J. S.; Lee, S. H.; Leem, J. Y. Temperature-Dependent Photoluminescence of Boron-Doped ZnO Nanorods. *Bull. Korean Chem. Soc.* **2013**, *34*, 3335−3339.

(22) Pati, S.; Majumder, S. B.; Banerji, P. Role of Oxygen Vacancy in Optical and Gas Sensing Characteristics of ZnO Thin Films. *J. Alloys Compd.* **2012**, *541*, 376−379.

(23) Zhou, X.; Xie, Z. X.; Jiang, Z. Y.; Kuang, Q.; Zhang, S. H.; Xu, T.; Huang, R. B.; Zheng, L. S. Formation of ZnO Hexagonal Micro-Pyramids: A Successful Control of the Exposed Polar Surfaces with the Assistance of An Ionic Liquid. *Chem. Commun.* **2005**, *44*, 5572−5574.

(24) Zhang, Z. H.; Lu, M. H.; Xu, H. R.; Chin, W. S. Shape-Controlled Synthesis of Zinc Oxide: A Simple Method for the Preparation of Metal Oxide Nanocrystals in Non-Aqueous Medium. *Chem.—Eur. J.* **2007**, *13*, 632−638.

(25) Gunawan, P.; Mei, L.; Teo, J.; Ma, J. M.; Highfield, J.; Li, Q. H.; Zhong, Z. Y. Ultrahigh Sensitivity of Au/1D alpha-Fe$_2$O$_3$ to Acetone and the Sensing Mechanism. *Langmuir* **2012**, *28*, 14090−14099.

(26) Kaneti, Y. V.; Yue, J.; Jiang, X. C.; Yu, A. B. Controllable Synthesis of ZnO Nanoflakes with Exposed (10$\bar{1}$0) for Enhanced Gas Sensing Performance. *J. Phys. Chem. C* **2013**, *117*, 13153−13162.

(27) Ahmad, M. Z.; Chang, J.; Ahmad, M. S.; Waclawik, E. R.; Wlodarski, W. Non-Aqueous Synthesis of Hexagonal ZnO Nano-pyramids: Gas Sensing Properties. *Sens. Actuators, B* **2013**, *177*, 286−294.

(28) Zeng, Y.; Zhang, T.; Yuan, M. X.; Kang, M. H.; Lu, G. Y.; Wang, R.; Fan, H. T.; He, Y.; Yang, H. B. Growth and Selective Acetone Detection Based on ZnO Nanorod Arrays. *Sens. Actuators, B* **2009**, *143*, 93−98.

(29) Li, X. D.; Chang, Y. Q.; Long, Y. Influence of Sn Doping on ZnO Sensing Properties for Ethanol and Acetone. *Mater. Sci. Eng., C* **2012**, *32*, 817−821.

(30) Wang, L. W.; Kang, Y. F.; Liu, X. H.; Zhang, S. M.; Huang, W. P.; Wang, S. R. ZnO Nanorod Gas Sensor for Ethanol Detection. *Sens. Actuators, B* **2012**, *162*, 237−243.

(31) Xue, X. Y.; Chen, Z. H.; Xing, L. L.; Ma, C. H.; Chen, Y. J.; Wang, T. H. Enhanced Optical and Sensing Properties of One-Step Synthesized Pt-ZnO Nano Flowers. *J. Phys. Chem. C* **2010**, *114*, 18607−18611.

(32) Alenezi, M. R.; Alshammari, A. S.; Jayawardena, K.; Beliatis, M. J.; Henley, S. J.; Silva, S. R. P. Role of the Exposed Polar Facets in the Performance of Thermally and UV Activated ZnO Nanostructured Gas Sensors. *J. Phys. Chem. C* **2013**, *117*, 17850−17858.

(33) Shi, Y. H.; Wang, M. Q.; Hong, C.; Yang, Z.; Deng, J. P.; Song, X. H.; Wang, L. L.; Shao, J. Y.; Liu, H. Z.; Ding, Y. C. Multi-Junction Joints Network Self-Assembled with Converging ZnO Nanowires as Multi-Barrier Gas Sensor. *Sens. Actuators, B* **2013**, *177*, 1027−1034.

(34) Han, N.; Wu, X. F.; Chai, L. Y.; Liu, H. D.; Chen, Y. F. Counterintuitive Sensing Mechanism of ZnO Nanoparticle Based Gas Sensors. *Sens. Actuators, B* **2010**, *150*, 230−238.

(35) Xie, J. A.; Li, Y. T.; Zhao, W.; Bian, L.; Wei, Y. Simple Fabrication and Photocatalytic Activity of ZnO Particles with Different Morphologies. *Powder Technol.* **2011**, *207*, 140−144.

(36) Wang, J. P.; Wang, Z. Y.; Huang, B. B.; Ma, Y. D.; Liu, Y. Y.; Qin, X. Y.; Zhang, X. Y.; Dai, Y. Oxygen Vacancy Induced Band-Gap Narrowing and Enhanced Visible Light Photocatalytic Activity of ZnO. *ACS Appl. Mater. Interfaces* **2012**, *4*, 4024−4030.

(37) Qin, H. C.; Li, W. Y.; Xia, Y. J.; He, T. Photocatalytic Activity of Heterostructures Based on ZnO and N-Doped ZnO. *ACS Appl. Mater. Interfaces* **2011**, *3*, 3152−3156.

(38) Zhang, L. X.; Zhao, J. H.; Lu, H. Q.; Gong, L. M.; Li, L.; Zheng, J. F.; Li, H.; Zhu, Z. P. High Sensitive and Selective Formaldehyde Sensors Based on Nanoparticle-Assembled ZnO Micro-Octahedrons Synthesized by Homogeneous Precipitation Method. *Sens. Actuators, B* **2011**, *160*, 364−370.

(39) Mani, G. K.; Rayappan, J. B. B. Novel and Facile Synthesis of Randomly Interconnected ZnO Nanoplatelets Using Spray Pyrolysis and Their Room Temperature Sensing Characteristics. *Sens. Actuators, B* **2014**, *198*, 125−133.

(40) Han, N.; Chai, L. Y.; Wang, Q.; Tian, Y. J.; Deng, P. Y.; Chen, Y. F. Evaluating the Doping Effect of Fe, Ti and Sn on Gas Sensing Property of ZnO. *Sens. Actuators, B* **2010**, *147*, 525−530.

(41) Chen, M.; Wang, Z. H.; Han, D. M.; Gu, F. B.; Guo, G. S. Porous ZnO Polygonal Nanoflakes: Synthesis, Use in High-Sensitivity NO$_2$ Gas Sensor, and Proposed Mechanism of Gas Sensing. *J. Phys. Chem. C* **2011**, *115*, 12763−12773.

(42) Han, N.; Hu, P.; Zuo, A.; Zhang, D. W.; Tian, Y. J.; Chen, Y. F. Photoluminescence Investigation on the Gas Sensing Property of ZnO Nanorods Prepared by Plasma-Enhanced CVD Method. *Sens. Actuators, B* **2010**, *145*, 114−119.

(43) Zhang, R.; Yin, P. G.; Wang, N.; Guo, L. Photoluminescence and Raman Scattering of ZnO Nanorods. *Solid State Sci.* **2009**, *11*, 865−869.

(44) Herring, N. P.; Almahoudi, S. H.; Olson, C. R.; El-Shall, M. S. Enhanced Photocatalytic Activity of ZnO-Graphene Nanocomposites Prepared by Microwave Synthesis. *J. Nanopart. Res.* **2012**, *14*, 1277.

(45) Gandhi, V.; Ganesan, R.; Syedahamed, H. H. A.; Thaiyan, M. Effect of Cobalt Doping on Structural, Optical, and Magnetic Properties of ZnO Nanoparticles Synthesized by Coprecipitation Method. *J. Phys. Chem. C* **2014**, *118*, 9715−9725.

(46) Fletcher, C.; Jiang, Y. J.; Sun, C. H.; Amal, R. Morphological Evolution and Electronic Alteration of ZnO Nanomaterials Induced by Ni/Fe Co-Doping. *Nanoscale* **2014**, *6*, 7312−7318.

(47) Husain, S.; Alkhtaby, L. A.; Bhat, I.; Giorgetti, E.; Zoppi, A.; Miranda, M. M. Study of Cobalt Doping on Structural and Luminescence Properties of Nanocrystalline ZnO. *J. Lumin.* **2014**, *154*, 430−436.

(48) Umar, A.; Kim, S. H.; Lee, Y. S.; Nahm, K. S.; Hahn, Y. B. Catalyst-Free Large-Quantity Synthesis of ZnO Nanorods by A Vapor-Solid Growth Mechanism: Structural and Optical Properties. *J. Cryst. Growth* **2005**, *282*, 131−136.

(49) Wong, K. W. J.; Field, M. R.; Ou, J. Z.; Latham, K.; Spencer, M. J. S.; Yarovsky, I.; Kalantar-zadeh, K. Interaction of Hydrogen with ZnO Nanopowders-Evidence of Hydroxyl Group Formation. *Nanotechnology* **2012**, *23*, 015705.

(50) Lv, J. P.; Li, C. D.; BelBruno, J. J. Defect Evolution on the Optical Properties of H^+-Implanted ZnO Whiskers. *CrystEngComm* **2013**, *15*, 5620−5625.

(51) Chen, M.; Wang, Z. H.; Han, D. M.; Gu, F. B.; Guo, G. S. High-Sensitivity NO_2 Gas Sensors Based on Fower-Like and Tube-Like ZnO Nanomaterials. *Sens. Actuators, B* **2011**, *157*, 565−574.

(52) Tiwari, P.; Srivastava, H.; Srivastava, A. K.; Deb, S. K. A Comparative Study on the Growth of ZnO Nanorods by Annealing Method in Different Environments. *J. Alloys Compd.* **2014**, *611*, 117−124.

(53) Al-Hardan, N. H.; Jalar, A.; Hamid, M. A. A.; Keng, L. K.; Shamsudin, R.; Majlis, B. Y. The Room-Temperature Sensing Performance of ZnO Nanorods for 2-methoxyethanol Solvent. *Sens. Actuators, B* **2014**, *203*, 223−228.

(54) Peng, Y.; Wang, Y.; Chen, Q. G.; Zhub, Q.; Xu, A. W. Stable Yellow ZnO Mesocrystals with Efficient Visible-Light Photocatalytic Activity. *CrystEngComm* **2014**, *16*, 7906−7913.

(55) Wang, L.; Li, H. B.; Xu, S. L.; Yue, Q. L.; Liu, J. F. Facet-Dependent Optical Properties of Nanostructured ZnO. *Mater. Chem. Phys.* **2014**, *147*, 1134−1139.

(56) Zhang, J. Y.; Cong, L.; Wan, H.; Wang, T. M. Green-Emission and N-Type Conductivity of ZnO: Zn Films Obtained Using Vapor Deposition Method. *Appl. Surf. Sci.* **2009**, *255*, 3530−3533.

(57) Gu, F. B.; Zhang, L.; Wang, Z. H.; Han, D. M.; Guo, G. S. Fine-Tuning the Structure of Cubic Indium Oxide and Their Ethanol-Sensing Properties. *Sens. Actuators, B* **2014**, *193*, 669−678.

(58) Can, M. M.; Shah, S. I.; Doty, M. F.; Haughn, C. R.; Firat, T. Electrical and Optical Properties of Point Defects in ZnO Thin Films. *J. Phys. D: Appl. Phys.* **2012**, *45*, 195104.

(59) Olive-Mendez, S. F.; Santillan-Rodriguez, C. R.; Gonzalez-Valenzuela, R. A.; Espinosa-Magana, F.; Matutes-Aquino, J. A. Role of Vanadium Ions, Oxygen Vacancies, and Interstitial Zinc in Room Temperature Ferromagnetism on $ZnO-V_2O_5$ Nanoparticles. *Nanoscale Res. Lett.* **2014**, *9*, 1−7.

(60) Janotti, A.; Van de Walle, C. G. Fundamentals of Zinc Oxide as A Semiconductor. *Rep. Prog. Phys.* **2009**, *72*, 126501.

(61) Cho, S.; Kim, D. H.; Lee, B. S.; Jung, J.; Yu, W. R.; Hong, S. H.; Lee, S. Ethanol Sensors Based on ZnO Nanotubes with Controllable Wall Thickness via Atomic Layer Deposition, An O_2 Plasma Process and An Annealing Process. *Sens. Actuators, B* **2012**, *162*, 300−306.